

# Annealing-Induced Hardening in Ultrafine-Grained and Nanocrystalline Materials

Jenő Gubicza

This paper is dedicated to Prof. Terence G. Langdon on the occasion of his 80th birthday

Annealing of deformed metals is considered as a process necessarily leading to softening due to the annihilation of lattice defects. However, in ultrafine-grained (UFG) and nanocrystalline materials, annealing at moderate temperatures may induce hardening. This review summarizes those effects that can result in annealing-induced hardening (AH) in fine-grained materials. It is noted that only those hardening phenomena are considered as AH effects that are not accompanied by the change of the phase composition and/or the grain size. Therefore, herein, strengthening caused by precipitation is not discussed. It is shown that heat treatment of nanomaterials can cause hardening due to the relaxation of grain boundaries and segregation of alloying elements to the grain boundaries as these effects hinder the occurrence of grain boundary sliding. For UFG metallic materials processed by severe plastic deformation techniques, the annihilation of mobile dislocations and the clustering of the remaining dislocations into low-angle grain boundaries during annealing can yield hardening. It is also shown that plastic deformation after annealing can cause a restoration of the yield strength and hardness to the same level as observed before annealing. The possible reasons of this deformation-induced softening effect are discussed in detail.

fault energy (SFE) materials also hardens the plastically deformed samples.<sup>[2,3]</sup> For large strains, plasticity leads to grain refinement that also contributes to hardening as suggested by the Hall-Petch equation.<sup>[4,5]</sup> The strengthening effect of plastic deformation is especially high when large strains are achieved by severe plastic deformation (SPD) techniques.<sup>[6]</sup> SPD methods applied at room temperature (RT) or in cryogenic conditions usually lead to ultrafine-grained (UFG) or nanocrystalline microstructures.<sup>[7]</sup> The maximum hardness is achieved at a grain size of about 20 nm, and further grain refinement may yield softening referred to as inverse Hall-Petch behavior.<sup>[8,9]</sup> This well-known phenomenon is caused by the change of deformation mechanisms from dislocation slip inside the grains to grain boundary sliding.<sup>[10,11]</sup> However, the grain size regime of the inverse Hall-Petch behavior usually cannot be reached by SPD techniques, i.e., deformation is believed to cause only strengthening.

## 1. Introduction

It is generally believed that plastic deformation yields hardening of metallic materials, whereas postdeformation annealing results in softening. Plastic straining of well-annealed coarse-grained polycrystalline metals leads to multiplication of dislocations, and the increase in dislocation density yields strength enhancement in accordance with the Taylor formula.<sup>[1]</sup> The formation of other defects such as stacking and twin faults in low stacking

Heat treatments of plastically strained metals can cause the annihilation of dislocations and grain growth due to recovery and recrystallization. These changes in the microstructure are generally considered to yield softening in accordance with the Taylor and Hall-Petch equations. Surprisingly, annealing may also cause hardening in plastically deformed coarse-grained metallic materials.<sup>[12–16]</sup> This phenomenon is referred to as annealing-induced hardening (AH) or simply anneal-hardening. It should be noted that the hardening caused by phase transformations (such as the formation of Guinier-Preston zones in Al alloys) is excluded from AH effects.

This overview aims to summarize the existing knowledge in the field of AH with a special emphasis on UFG and nanocrystalline materials. First, the reasons of the effect of AH in coarse-grained materials are discussed. Then, the mechanisms of AH in UFG and nanomaterials are overviewed. The results obtained on samples processed by “bottom-up” and “top-down” techniques are discussed in separate sections.

Prof. J. Gubicza  
Department of Materials Physics  
Eötvös Loránd University  
P.O.B.32, Budapest H-1518, Hungary  
E-mail: jeno.gubicza@ttk.elte.hu

 The ORCID identification number(s) for the author(s) of this article can be found under <https://doi.org/10.1002/adem.201900507>.

© 2019 The Authors. Published by WILEY-VCH Verlag GmbH & Co. KGaA, Weinheim. This is an open access article under the terms of the Creative Commons Attribution-NonContribution License, which permits use, distribution and reproduction in any medium, provided the original work is properly cited and is not used for commercial purposes.

DOI: 10.1002/adem.201900507

## 2. Anneal-Hardening in Coarse-Grained Materials

In the case of coarse-grained metallic materials, AH was found to occur only in alloys at heat treatment temperatures lower than

the recrystallization temperature, typically near the homologous temperature of 0.3–0.4. The phenomenon of AH for coarse-grained materials was studied mainly on Cu alloys, such as Cu(Al) solid solutions.<sup>[16]</sup> For these alloys, the effect of AH was observed in the temperature range of 423–523 K.<sup>[15]</sup> The first pioneering studies on AH were published in 1950's and 1960's.<sup>[15,17]</sup> The term “anneal-hardening” was proposed by Hasiguti.<sup>[17]</sup> The following features of AH were identified in plastically deformed coarse-grained materials:<sup>[13,14]</sup> 1) The higher the preliminary plastic strain before annealing, the higher the effect of AH. 2) The higher the concentration of substitutional alloying elements, the higher the effect of AH. 3) The higher the difference between the atomic radii of solute and solvent elements, the higher the effect of AH. 4) The relative flow stress increase caused by annealing decreases with increasing the strain at which the flow stress is measured.

These experimental observations suggested that AH in coarse-grained materials are mainly caused by the segregation of solute atoms to dislocations during annealing. In the case of Cu(Al) solid solutions with low SFE, the segregation of Al to stacking faults during annealing may also contribute to hardening.<sup>[15]</sup> This segregation also occurs at the stacking fault ribbon of extended dislocations. It should be noted that this segregation may result in local ordering, e.g., the formation of ordered Cu<sub>3</sub>Al phase, which may also contribute to hardening.<sup>[16]</sup>

It was also shown that grain boundaries usually play a crucial role in AH in coarse-grained materials.<sup>[13]</sup> Namely, this effect did not occur in single crystal Cu – 13.5 at% Al alloy strained by tension to ≈9%, whereas significant AH was observed in bicrystal and polycrystalline (the grain size was 34 μm) specimens with the same chemical composition and subjected to the same prestraining. Hardness profile measurements along a line perpendicular to the grain boundary in a Cu – 13.5 at% Al bicrystal revealed that annealing at temperatures between 373 and 523 K resulted in a 10% increase in the hardness from ≈1000 to ≈1100 MPa in the vicinity of the grain boundary, while this effect decreased to a marginal level at a distance of 300 μm from the boundary.<sup>[13]</sup> The AH effect was observed only for one side of the bicrystal containing edge dislocation pile ups. The other side with screw dislocation pile-ups exhibited softening after the same heat treatments. These observations suggested that AH was caused by the segregations of solute atoms to edge dislocations in the pile-ups formed in the vicinity of the grain boundary of the bicrystal. The pinning effect of the segregated solutes on the motion of edge dislocations resulted in AH. Thus, the crucial role of grain boundaries in AH in coarse-grained materials is the creation of pile-ups with high dislocation density. For polycrystalline Cu – 13.5 at% Al solid solution (with the grain size of 34 μm) prestrained by tension for the strain of ≈9%, AH resulted in a hardness increase of about 8% from 1250 to 1350 MPa.<sup>[13]</sup> Solute atom segregation to dislocations during annealing also caused AH in coarse-grained dilute Mg – 0.3 at% Zn – 0.1 at% Ca alloy.<sup>[18]</sup> This effect was observed only after predeformation for a strain of about 2% before annealing. In this material, the heat treatment at 473 K for 1 h resulted in a 20% increase of the yield strength from 110 to 132 MPa. The same increase in hardness was achieved at lower temperatures (353 and 423 K); however, the necessary time of annealing was higher (24 and 168 h at 353 and 423 K, respectively). The effect of AH diminished



**Jenő Gubicza** is a professor in Department of Materials Physics, at Eötvös Loránd University, Budapest, Hungary. He also serves as the Head of the Physics Doctoral School of his university. His special field is the study of the correlation between the microstructure and the mechanical properties of nanomaterials. He wrote three books about the defect structure and properties of nanomaterials as well as about X-ray line profile analysis, which is an effective method for the study of the defect structure of nanomaterials.

during repetitive application of deformation and annealing in Mg – 0.3 at% Zn – 0.1 at% Ca alloy.<sup>[18]</sup> It is important to note that AH was not observed in coarse-grained pure metals.

The change of crystallographic texture during annealing of plastically deformed materials may also cause AH.<sup>[19]</sup> This effect was observed in coarse-grained AZ31 Mg alloy processed by rolling and additional compression. **Figure 1** shows the change of texture during rolling and subsequent compression. First, cold rolling with 7% thickness reduction was performed on a recrystallized AZ31 sheet with a grain size of about 16 μm. This processing step resulted in a (00.2) texture in normal direction (ND) (Figure 1). The subsequent compression for a strain of 2% along transverse direction (TD) led to extension twinning on planes (10.2).<sup>[19]</sup> This deformation mechanism is preferred if the hexagonal c-axis (i.e., direction [00.2]) is perpendicular to the compression direction since in this case the Schmid factor of extension twinning is the highest.<sup>[20]</sup> This twinning process corresponds to a rotation of direction [00.2] with an angle of 86°. Therefore, a part of (00.2) texture in direction ND turned into (00.2) texture in direction TD as shown in Figure 1. This sample is regarded as the deformed material in this study. Annealing of this specimen at temperatures between 473 and 623 K for 0.5–3 h resulted in recrystallization that removed (10.2) extension twins from the microstructure and restored (00.2) texture in direction ND.<sup>[19]</sup> The change of the texture during annealing led to different deformation mechanisms in the deformed and annealed specimens

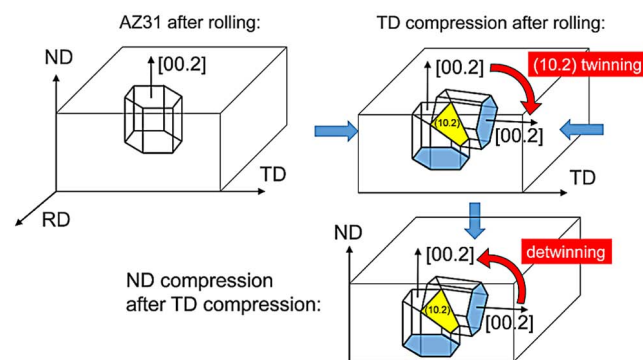


**Figure 1.** The change of texture in coarse-grained AZ31 Mg alloy during rolling and subsequent compressions in TD and ND directions. Data were taken from the references<sup>[19]</sup>

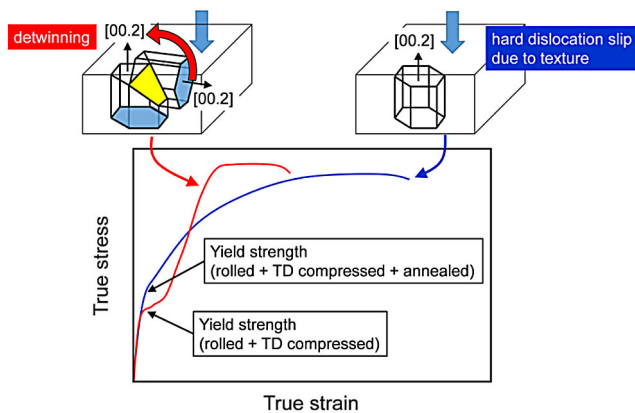


**Figure 2.** A schematic illustrating the compressive stress–strain curves for AZ31 alloy processed by a combination of rolling and compression along axis TD, as well as for the sample annealed after TD compression. The compression for both specimens was performed along axis ND. Reproduced with permission.<sup>[19]</sup> Copyright 2016, Elsevier.

during compression in direction ND. **Figure 2** shows that in the deformed sample detwinning was the main deformation mechanism in the beginning of compression in ND direction since the regions twinned in the preliminary TD compression had a high Schmid factor for twinning back to the original crystallographic direction (i.e., for detwinning). The occurrence of detwinning was also indicated by the plateau on the stress–strain curve after yielding. During detwinning process, the existing twin boundaries are migrating without new twin nucleation; therefore, detwinning requires low stress. In contrast, in the annealed sample ND compression was carried out parallel to the crystallographic (00.2) direction. Therefore, extension twinning/detwinning did not occur and dislocation glide in the  $\langle a \rangle$  and  $\langle c+a \rangle$  dislocation slip systems must have been activated during ND compression. However, the slip of  $\langle a \rangle$  dislocations is difficult due to (00.2) texture, and  $\langle c+a \rangle$  dislocations have large critical resolved shear stress.<sup>[19]</sup> Thus, annealing resulted in an increase in yield strength as shown schematically in Figure 2. It should be noted that the ultimate tensile strength was not higher for the annealed AZ31 sample than that for the deformed material since the easy detwinning occurred only in the beginning of compression of the predeformed specimen. A former study has shown that even a compressive strain of 3% in direction ND is enough for complete detwinning.<sup>[21]</sup>

It is also worth noting that AH was also observed in coarse-grained AZ31 alloy when the temperature and duration of heat treatment was only 443 K and 15 min, respectively, i.e., recrystallization did not occur and (10.2) twins remained in the microstructure even after annealing.<sup>[21]</sup> In this case, the phenomenon of AH was caused by the segregation of Al and Zn atoms to twin boundaries. Detwinning occurred by the motion of twin boundaries in both the prestrained and the annealed samples; however, the segregated solute atoms pin twin boundaries in the annealed material, thereby resulting in AH. The significance of solute segregation in the AH effect was also shown by the fact that similar heat treatment in twinned pure magnesium did not lead to hardening.<sup>[21]</sup> Segregation of Gd and Zn solute atoms to twin boundaries was observed in Mg

alloys annealed after 2–3% compression even if the twin boundaries are coherent.<sup>[22]</sup> The periodic distribution of solute elements on coherent twin boundaries reduced the lattice strains along twin boundaries. The large (e.g., Gd) and small (e.g., Zn) atoms occupied extension and compression sites in the twin boundaries. Then, both the twin boundary energy and the strain energy in the grain interiors caused by the solute atoms decreased. The segregation of alloying elements to twin boundaries impeded twin boundary motion during subsequent deformation, resulting in the AH effect.<sup>[22]</sup> Namely, the yield strength increased by 20% from 75 to 90 MPa in the preliminary compressed Mg – 0.2 at% Gd alloy (the strain was 2.5%) after annealing at 423 K for 3 h. The significance of Gd segregation to twin boundaries in the AH effect was also revealed in coarse-grained Mg – 10% Gd – 3% Y – 0.3% Zr alloy.<sup>[23]</sup>

The demand for strength enhancement induced the development of novel manufacturing techniques of UFG and nanocrystalline materials.<sup>[7,9,24]</sup> These processing methods can be classified as “bottom-up” and “top-down” approaches. In the former methods, the UFG or nanomaterials are assembled from atoms or molecules while during the latter procedures the fine-grained microstructures are achieved by SPD-processing of coarse-grained bulk materials. Both groups of techniques yield very high defect densities in the as-processed samples. After overviewing the effect of AH in coarse-grained materials, the question naturally arises whether annealing of UFG and nanomaterials at moderate temperatures may result in an additional hardening, and due to the higher defect density this AH effect is higher or not than in the coarse-grained counterparts. In the next sections, the existing knowledge in the field of AH for UFG and nanocrystalline materials is summarized. Individual sections are devoted to samples processed by “bottom-up” and “top-down” techniques. Moreover, another interesting effect, the so-called “deformation-induced softening” in anneal-hardened materials will also be discussed in an additional section. This phenomenon implies the decrease of strength in UFG and nanomaterials during plastic deformation. This effect is also referred to as “work softening” or “deformation softening” (DS). The latter name will be used throughout this overview.

### 3. Annealing-Induced Hardening in Ultrafine-Grained and Nanocrystalline Materials

The first studies on the phenomenon of AH in UFG and nanocrystalline materials were published in the early 1990s.<sup>[25–27]</sup> In these studies, an Al-1.5%Mg solid solution and a Ni<sub>3</sub>Al intermetallic compound were studied. First, these materials were processed by high pressure torsion (HPT) SPD technique to the equivalent strain of  $\approx 7$  at RT. HPT-processing yielded a grain size of 150 and 50 nm for Al-1.5% Mg and Ni<sub>3</sub>Al, respectively.<sup>[25,27]</sup> For both alloys, annealing at the homologous temperature of  $\approx 0.37$  for 30 min resulted in 13% and 32% higher hardness than the initial value for the HPT-processed Al-1.5% Mg and Ni<sub>3</sub>Al samples, respectively. This homologous temperature corresponds to 373 and 623 K for Al – 1.5% Mg and Ni<sub>3</sub>Al, respectively.<sup>[25,27]</sup> It was proposed that AH was caused by the relaxation of grain boundaries during annealing. In the HPT-processed samples, there was a high fraction of nonequilibrium

boundaries. During the heat treatment at the homologous temperature of 0.37, the boundaries were relaxed and their Hall-Petch hardening effect became higher. The term “grain boundary relaxation” means that the excess defects in the grain boundaries are annihilated and the boundary structure becomes more equilibrated. The effect of AH on hexagonal Ti with 99.53% purity processed by HPT was also demonstrated at the end of 1990s.<sup>[28]</sup> A heat treatment at 523 K (corresponding to the homologous temperature of 0.27) for 2 h resulted in an increase of ultimate tensile strength from 1500 to 1700 MPa, while the grain size remained practically unchanged ( $\approx 80$  nm). In this case, AH was explained again by the relaxation of grain boundaries in the UFG microstructure. It is noted that an increase in the yield strength was not observed for this Ti sample. In this case, the mechanical properties were determined by a three-point bending test. During bending, the deformation is not uniform in the specimen, i.e., the plastic flow occurs first at the compressed and stretched surfaces of the sample while the middle

of the beam deforms only elastically. As a result, the determination of the onset of plasticity (i.e., the yield strength) is uncertain; therefore, the AH effect may not be revealed.

In the last 20 years, the effect of AH was studied in detail for different pure metals and alloys processed either by bottom-up or top-down approaches. According to the literature, the following possible reasons of AH were indentified: 1) grain boundary relaxation; 2) annihilation of mobile dislocations; 3) reduction of the densities of easy dislocation sources; 4) arrangement of dislocations into “hard” configurations; 5) formation of vacancy clusters from excess vacancies; 6) segregation of solute atoms to dislocations; 7) segregation of solute atoms to twin faults; 8) segregation of solute atoms to grain boundaries; 9) formation of stacking and twin faults; and 10) development of “hard” texture.

In the following sections, first the phenomenon of AH will be discussed for SPD-processed UFG materials, then the results obtained for this effect in nanomaterials fabricated by bottom-up methods will be presented. **Table 1** lists the relative increase

**Table 1.** The relative hardening observed after annealing of different UFG and nanomaterials. The processing of the samples was usually carried out at RT. If other temperature was applied, it is indicated in the column “Processing method.” The grain sizes of the samples obtained by electron microscopy are also shown. For some samples, the duration of annealing is not shown as in these cases the material was heated up to the given temperature in differential scanning calorimetry (DSC) at  $40 \text{ K min}^{-1}$  and then quenched to RT.

Material	Grain size [nm]	Processing method	Annealing conditions	Yield strength or hardness before annealing [MPa]	Relative hardening [%]	Reference
Samples processed by top-down approaches						
99.99% Al	N.A.	6 ARB	423 K, 30 min	N.A.	9	[29]
99.99% Al	690	6 ARB	448 K, 30 min	97	7	[30]
99.7% Al	345	12 CR <sup>a)</sup>	423 K, 30 min	167	8	[31]
99.7% Al	345	12 CR	EPA <sup>a)</sup> , 2 min	167	14	[31]
99.5% Al	N.A.	6 ECAP	383 K, 4 h	142	9	[32]
99.5% Al	N.A.	7 ECAP	353 K, 4 h	142	8	[32]
99.2% Al	180	6 ARB	423 K, 30 min	259	8	[33]
Al-1.5%Mg	150	HPT ( $\epsilon = 7$ )	373 K, 30 min	1500 <sup>b)</sup>	13	[25]
99.99% Ni	300	ED <sup>a)</sup> + rolling at LNT	547 K, 5 min	2730 <sup>b)</sup>	5	[34]
Ni-1.3% (Mo, Al, Fe)	130	20 HPT	600 K	970	19	[35]
Ni-8.6% (Mo, Al, Fe)	130	20 HPT	630 K	1367	3	[35]
Ni-1%Fe	15	MA <sup>a)</sup>	623 K, 1 h	6100 <sup>b)</sup>	3	[36]
Ni-10%Fe	N.A.	MA	523 K, 1 h	6100 <sup>b)</sup>	7	[36]
Cu-7%Al	63	6 HPT	523 K, 2 h	3100 <sup>b)</sup>	5	[37]
Cu-12.1%Al-4.1%Zn	30	Rolling at LNT	473 K, 1 h	2700 <sup>b)</sup>	11	[38]
Cu-12.1%Al-4.1%Zn	N.A.	Rolling at LNT	473 K, 1 h	768	9	[39]
Cu-12.1%Al-4.1%Zn	N.A.	CR	473 K, 1 h	720	11	[39]
Cu-4.3%Al-22.8%Zn	37	Rolling at LNT	473 K, 1 h	2300 <sup>b)</sup>	15	[38]
Cu-30%Zn-5%Zr	N.A.	Milled at LNT	473 K, 1 h	3200 <sup>b)</sup>	34	[40]
CoCrNi	126	3 ECAP	773 K, 1 h	1191	9	[41]
CoCrNi	40	5 HPT	773 K, 1 h	6090 <sup>b)</sup>	26	[42]
CoCrFeMnNi	N.A.	CR	773 K, 1 h	3940 <sup>b)</sup>	9	[43]
Ni <sub>3</sub> Al	50	HPT ( $\epsilon = 7$ )	623 K, 30 min	6130 <sup>b)</sup>	32	[27]
Fe-10%Ni	N.A.	MA	473 K, 1 h	7600 <sup>b)</sup>	12	[36]
Fe-4%Al-11%Si	10	MA	723 K, 1 h	9800 <sup>b)</sup>	17	[36]
99.98% Mg	3000	3 HE	573 K, 6 h	98	28	[44]

**Table 1.** Continued.

Material	Grain size [nm]	Processing method	Annealing conditions	Yield strength or hardness before annealing [MPa]	Relative hardening [%]	Reference
99.98% Mg	3000	1 HE + 1 CD <sup>a)</sup>	473 K, 6 h	127	18	[44]
CP-Ti	80	15 ASR + 4 SR <sup>a)</sup>	473 K, 20 min	805	4	[45]
CP-Ti	120	HPT ( $\epsilon = 7$ )	573 K, 10 min	800	25	[46]
Zn-22% Al	400	Rolling at RT	523 K, 1.5 h	195 <sup>b)</sup>	162	[47]
Zn-22%Al-0.3%Cu	300	Rolling at RT	523 K, 30 min	420 <sup>b)</sup>	90	[47]
Samples processed by bottom-up approaches						
Ni	30	ED	423 K, 1 h	839	10	[48]
Ni	30	ED	473 K, 1 h	4300 <sup>b)</sup>	15	[49]
Ni	15	ED	473 K, 1 h	6800 <sup>b)</sup>	18	[50]
Ni-1.2%P	10	ED	673 K, 1 h	6500 <sup>b)</sup>	47	[51]
Ni-2.8%Mo	13	ED	623 K, 1 h	5800 <sup>b)</sup>	28	[49]
Ni-9.1%Mo	9	ED	683 K, 1 h	5800 <sup>b)</sup>	46	[49]
Ni-12.7%Mo	6	ED	713 K, 1 h	5500 <sup>b)</sup>	70	[49]
Ni-18.7%Mo	4	ED	783 K, 1 h	5200 <sup>b)</sup>	110	[49]
Ni-21.5%Mo	3	ED	798 K, 1 h	5000 <sup>b)</sup>	126	[49]
Ni-1%Fe	16	ED	479 K, 1 h	5950 <sup>b)</sup>	3	[52]
Ni-15%Fe	9	ED	523 K, 1.5 h	1587	16	[53]
Ni-23%Fe	22	ED	523 K, 1.5 h	1710	27	[54]
Ni-5%W	N.A.	ED	673 K, 1 h	5600 <sup>b)</sup>	16	[55]
Ni-15%W	N.A.	ED	673 K, 1 h	5600 <sup>b)</sup>	11	[55]
Ni-21%W	3	ED	573 K, 1 h	7700 <sup>b)</sup>	20	[56]
Cu-10%Nb	25	MS	573 K, 1 h	5100 <sup>b)</sup>	3	[57]

<sup>a)</sup>CR, cold rolling; ASR, asymmetric rolling; SR, symmetric rolling; CD, cold drawing; MA, mechanical alloying by ball milling; MS, magnetron sputtering; EPA, electric pulse annealing; ED, electrodeposition; <sup>b)</sup>The hardness values.

of yield strength or hardness due to AH for both groups of materials. It should be emphasized that those processes are regarded as AH effects that result in hardening during annealing without significant changes in the grain size and/or the phase composition.

### 3.1. Strengthening Caused by the Heat Treatment of SPD-Processed UFG Materials

Annealing of SPD-processed UFG or nanocrystalline materials may yield a considerable strengthening.<sup>[29,35,37,48,49,51,58]</sup> There may be many reasons of this hardening such as annihilation of mobile dislocations or formation of precipitates in supersaturated solid solutions during SPD-processing.<sup>[59–61]</sup> However, only those phenomena are regarded as AH effects that do not involve phase transformation. The possible reasons of AH are listed earlier. The homologous temperature of the maximum achievable hardness or yield strength was different for the various materials; however, for the majority of SPD-processed samples, it was between 0.35 and  $0.45 \times T_m$ , where  $T_m$  is the melting point.<sup>[25,27,31–33,35,38,39]</sup> This range corresponds to the temperatures of about 400–600 K. Due to the moderate temperatures of AH, grain growth and recrystallization are usually avoided.

One possible reason of AH is the annihilation of mobile dislocations and the clustering of the remaining dislocations into low energy hard configurations, such as low angle grain boundaries or dipolar dislocation walls. For instance, for UFG Ni – 1.3 wt% (Mo, Al, Fe) alloy processed by HPT at RT heating up to 600 K in a calorimeter yielded an increase of the yield strength from 970 to 1140 MPa, which corresponds to an enhancement of 19% (see also Table 1).<sup>[35]</sup> The ultimate tensile strength also increased by 13% from 1370 to 1570 MPa. These changes in the strength were above the experimental error of the measurements. The tensile engineering stress–strain curves for the HPT-processed alloy and the sample heated up to 600 K are shown in **Figure 3**. This temperature corresponds to the beginning of the main exothermic DSC peak in the thermogram taken by calorimetry (see also **Figure 3**). For this Ni alloy, 600 K is equivalent to the homologous temperature of 0.35. This heat treatment did not cause either precipitation or grain growth. The grain size was  $\approx 180$  nm in the HPT-processed sample that remained unchanged after heating up to 600 K as shown in **Figure 4**. In contrast, the dislocation density decreased from  $\approx 27 \times 10^{14}$  to  $\approx 17 \times 10^{14} \text{ m}^{-2}$  due to recovery. In addition, the remaining dislocations were rearranged into a more clustered configuration as suggested by the decrease of the dislocation arrangement parameter (**Figure 4**). This parameter can be determined by X-ray

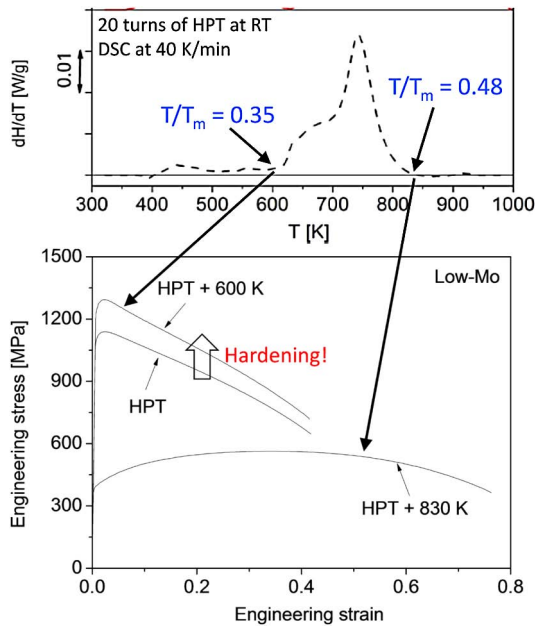


**Figure 3.** Tensile engineering stress–strain curves for the HPT-processed Ni – 1.3 wt% (Mo, Al, Fe) alloy and the samples heated up to 600 and 830 K. Reproduced with permission.<sup>[35]</sup> Copyright 2018, Wiley. The former and the latter temperatures correspond to the beginning and the end of the main exothermic DSC peak shown at the top of the figure. Reproduced with permission.<sup>[62]</sup> Copyright 2017, Elsevier.

diffraction line profile analysis and describes the degree of mutual shielding of the strain fields of dislocations.<sup>[63]</sup> The value of the dislocation arrangement parameter decreases if the dislocations are arranged into low energy configurations such as dipolar dislocation walls or low angle grain boundaries. The

clustering of dislocations into boundaries during annealing to 600 K was also confirmed by the increase in the fraction of low angle grain boundaries from 23% to 41% as revealed by electron backscatter diffraction (EBSD) experiments.<sup>[35]</sup> The variation of the low-angle grain boundary fraction and the schematic change of the arrangement of dislocations are also shown in Figure 4. It was shown formerly that clustered dislocation structures, such as low angle grain boundaries and dipolar walls, have a higher strengthening effect than that of a randomly distributed dislocation ensemble. This effect was manifested in the increase of the value of parameter  $\alpha$  in the Taylor equation when the random dislocation structure is clustered. This parameter characterizes the hardening of a unit dislocation density. Therefore, the more clustered dislocation structure in the sample annealed at 600 K has a higher hardening effect. In addition, most probably, mainly the mobile dislocations were annihilated during annealing at 600 K, which made the subsequent plastic deformation more difficult.<sup>[29]</sup> Thus, the annihilation of dislocations during heat treatment might have also contributed to AH. In addition, the relaxation of nonequilibrium high-angle grain boundaries during annealing may yield a more difficult emission of dislocations from the boundaries, and this effect may also result in hardening.<sup>[58]</sup> Figure 3 also reveals that if the HPT-processed UFG Ni – 1.3 wt% (Mo, Al, Fe) sample was heat treated up to the end of the main exothermic DSC peak (830 K), softening occurred due to recrystallization, which was accompanied by the decrease in the dislocation density below  $10^{13} \text{ m}^{-2}$  and a grain growth from  $\approx 180$  to  $\approx 870$  nm. For this material, 830 K corresponds to the homologous temperature of about 0.48.

The influence of the increase of the solute content on AH was also studied in the HPT-processed Ni(Mo,Al,Fe) alloy.<sup>[35]</sup> The Mo concentration was enhanced from about  $\approx 0.3$  to  $\approx 5$  at%, leading to the composition of Ni – 8.6 wt% (Mo, Al, Fe). The increase in

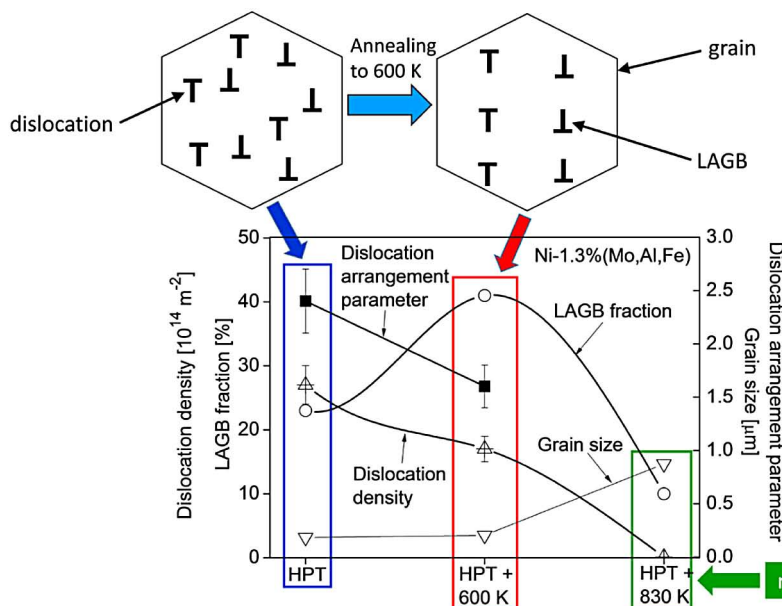


**Figure 4.** Evolution of the grain size, the dislocation density, the dislocation arrangement parameter, and the fraction of low-angle grain boundaries (LAGBs) for Ni – 1.3 wt% (Mo, Al, Fe) alloy processed by HPT and subsequently heated up to 600 and 830 K. The schematics above this diagram illustrate the arrangement of dislocations into LAGBs without grain-growth during annealing at 600 K. Reproduced with permission.<sup>[35]</sup> Copyright 2018, Wiley.

solute concentration led to an enhancement of the dislocation density to  $\approx 59 \times 10^{14} \text{ m}^{-2}$  and a reduction of the grain size to  $\approx 130 \text{ nm}$ .<sup>[62]</sup> Due to the stabilization effect of alloying elements, the main exothermic DSC peak started at higher temperature (630 K). Although, heating of the HPT-processed sample to this temperature yielded AH, the increase in the yield strength was only 2.4% from 1367 to 1400 MPa. The improvement of the ultimate tensile strength was also smaller (8%) than for the alloy with a lower solute content.<sup>[35]</sup> The lower AH can be explained by the hindering effect of solute atoms on the rearrangement of dislocations into low-angle grain boundaries during annealing.

Unlike for coarse-grained materials, in the case of SPD-processed UFG materials, the AH may also occur in very dilute alloys and pure samples such as Al, Mg, and Ti.<sup>[31,44,45,64]</sup> In pure SPD-processed materials, there is a high density of dislocations; therefore, the annihilation of its mobile fraction and the clustering of the remaining dislocations have a significant effect on strength. In addition, due to the UFG microstructure, there is a high amount of grain boundaries; therefore, their relaxation can cause considerable hardening since the emission of dislocation from relaxed boundaries is more difficult than from non-equilibrium boundaries. For instance, AH was observed in UFG aluminum with 99.7% purity processed by 12 passes of cold rolling, which corresponded to an equivalent strain of 4.9.<sup>[31]</sup> Prior to each pass of rolling, the sample was immersed into liquid nitrogen. The average grain size of the as-processed material was about 350 nm. It should be noted that the grains were elongated due to rolling. Two different methods were used for annealing: 1) traditional air furnace annealing at 423 K for 30 min and 2) electric pulse annealing with  $500 \text{ A cm}^{-2}$  average current density for 2 min. In the latter case, the temperature of the sample increased to 400–423 K. Electric pulse annealing did not change the grain size while after furnace annealing the grain size increased to about 450 nm. Electric pulse and the furnace annealing processes resulted in an increase in the yield strength by 14% and 8%, respectively (see also Table 1), which was explained by the annihilation of mobile dislocations and the reduction of the number of easy dislocation sources. It should be noted that a higher hardening was achieved in a shorter time by electric pulse annealing since the electric pulses promoted the recovery of the dislocation structure.<sup>[31]</sup>

AH was also observed in commercially pure Al samples with 99.5% (1050 series) and 99.2% (1100 series) purities.<sup>[32,33]</sup> In the former case, the Al samples were processed by 6 and 7 passes of equal channel angular pressing (ECAP) at RT.<sup>[32]</sup> Annealing for 4 h at 383 and 353 K for 6 and 7 passes, respectively, resulted in a maximum in the yield strength versus temperature diagram. This maximum is 8–9% higher than the yield strength (142 MPa) of the ECAP-processed material (Table 1). This AH effect was explained by the clustering of excess vacancies in the SPD-processed samples during annealing. These clusters can hinder the motion of dislocations, thereby resulting in hardening. The AH effect was also observed in Al with 99.2% purity processed by 6 passes of accumulative roll bonding (ARB) at RT.<sup>[33]</sup> Annealing at 423 K for 30 min resulted in an 8% increase in the yield strength (Table 1). This phenomenon was explained by the annihilation of mobile dislocations. Indeed, the dislocation density decreased from  $\approx 1.3$  to  $\approx 0.5 \times 10^{14} \text{ m}^{-2}$ , and most probably, mainly the mobile dislocations were annihilated. It is

noted that the same relative strengthening (the yield strength increased by 9%) was observed for 4N purity Al SPD-deformed and annealed under the same conditions as applied for 99.2% purity Al.<sup>[29]</sup> Annealing of the ARB-processed 4N purity Al at a slightly higher temperature of 448 K for 30 min led to a similar increase in the yield strength (7%).<sup>[30]</sup> This indicates that AH may occur even in pure metals if they are processed by SPD.

The effect of AH was also observed in SPD-processed pure hexagonal structures such as Mg with 99.98% purity. A Mg material was deformed by 3 passes of cold hydrostatic extrusion (HE) to the equivalent strain of 3.2, resulting in a grain size of 2–3  $\mu\text{m}$ .<sup>[44]</sup> The yield strength of the SPD-processed pure Mg samples increased by 28% during annealing at 573 K for 6 h (Table 1). An additional sample was processed by 1 pass of HE and subsequent cold drawing. This combined SPD-processing also resulted in an equivalent strain of 3.2 and the same grain size of 2–3  $\mu\text{m}$ . However, the yield strength of the latter sample (127 MPa) was higher than the value obtained for the specimen processed by 3 passes of HE (98 MPa). For the material processed by the combined SPD-processing, annealing at 473 K for 6 h led to an increase of the yield strength by 18%. The AH effect for both Mg samples was explained by the thermally activated extension of the cores of  $\langle c+a \rangle$  pyramidal edge dislocations in the basal plane of Mg.<sup>[44]</sup> This dislocation dissociation increased the yield strength due to self-blocking of  $\langle c+a \rangle$  dislocations.<sup>[65]</sup> Similar to the yield strength, the ultimate tensile strength also increased while the elongation to failure only slightly decreased or remained unchanged.<sup>[44]</sup>

Commercially pure (Grade 2) Ti with a hexagonal structure also exhibited AH after SPD-processing.<sup>[45]</sup> SPD was performed using a combination of asymmetric rolling for 15 passes (corresponds to an 83% thickness reduction) and symmetric rolling for 4 passes (corresponds to an 80% thickness reduction) at RT. The rolled Ti with the grain size of 80 nm was annealed at 473 K for 20 min, which resulted in an increase in the yield strength by 4% (Table 1). The effect of AH was explained by the annihilation of mobile dislocations and the ordering of the remaining dislocations into “hard” clustered configurations as discussed earlier. It is noted that the homologous temperature of this AH phenomenon was relatively low ( $0.24 \times T_m$ ). For HPT-processed Ti, the AH effect was observed at a higher homologous temperature of  $0.30 \times T_m$ .<sup>[46]</sup> Annealing resulted in an increase in the yield strength from about 800 to  $\approx 1000$  MPa, corresponding to an enhancement of 25% (Table 1). The ultimate tensile strength was improved similarly. In addition, the elongation to failure was improved from 12% to 20% due to annealing. This is an exceptional behavior as AH usually results in an unchanged or slightly lower ductility as compared with the SPD-processed state. The AH effect was attributed to the annihilation of mobile dislocations and the ordering of the remaining ones at the grain boundaries. **Figure 5** shows schematically the specific arrangement of dislocations observed by high-resolution transmission electron microscopy (HRTEM) at a grain boundary after the heat treatment of the HPT-processed Ti.<sup>[46]</sup>

The effect of AH was also observed in 99.99% pure Cu and Ni with UFG microstructures.<sup>[34]</sup> These materials were processed by the combination of electrodeposition and subsequent rolling at liquid nitrogen temperature (LNT) to a thickness reduction of 95%. The grain sizes in the UFG Cu and Ni were 200 and

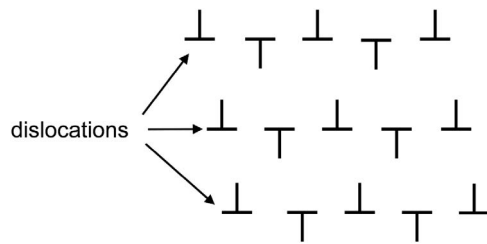


**Figure 5.** A schematic showing the specific arrangement of dislocations observed by HRTEM at a grain boundary after the heat treatment of a HPT-processed Ti at 473 K for 20 min. Data were taken from the references<sup>[46]</sup>

300 nm, respectively. In addition, some grains in Cu contained twin lamellas with a thickness of 20 nm. These twins might be formed either during rolling at LNT or by self-annealing during the transmission electron microscopy (TEM) sample preparation at RT. Such twins were not observed in Ni due to the much higher SFE as compared with Cu. The cryolled samples were annealed at different temperatures for 5 min.<sup>[34]</sup> First, the hardness decreased with increasing annealing temperature; however, at 464 and 547 K for Cu and Ni, respectively, a peak was observed on the hardness-temperature curve. It should be noted that for Ni the hardness corresponding to this peak was only 5% higher than that for the non-annealed state, whereas for Cu this was only a local maximum and the hardness corresponding to the peak was 26% lower than the value measured on the deformed sample. Therefore, in the latter case, the effect cannot be regarded as AH, and the corresponding data were not listed in Table 1. Anyway, the local hardness increase was explained by the development of small twins in the early stage of recrystallization.<sup>[34]</sup> It is noted that similar peak was observed on the yield strength versus temperature diagram at 423 K for ECAP-processed 1100 and 3004 Al alloys.<sup>[66]</sup>

Alloying of Cu can result in a change of the mechanism of AH. It was shown that in strongly alloyed Cu-Al-Zn solid solutions the effect of AH was mainly caused by the solute segregation to lattice defects and the formation of twin and stacking faults during annealing.<sup>[38,39]</sup> The same effect was observed for a HPT-processed Cu-7%Al alloy.<sup>[37]</sup> The significant contribution of planar faults to hardening can be attributed to the low SFE of these alloys. For instance, the SFE of Cu – 12.1% Al – 4.1% Zn alloy is  $\approx 7 \text{ mJ m}^{-2}$ , while for Cu – 4.3% Al – 22.8% Zn alloy this value is  $\approx 10 \text{ mJ m}^{-2}$ . These alloys were rolled at LNT to the thickness reduction of 96%, leading to the grain sizes of  $\approx 30$  and  $\approx 37$  nm for the former and the latter materials, respectively.<sup>[38]</sup> Annealing at 473 K for 1 h resulted in a hardness increase of 11% and 15% for Cu – 12.1% Al – 4.1% Zn and Cu – 4.3% Al – 22.8% Zn alloys, respectively (Table 1). It was also shown that the AH effect on the yield strength was similar (9–11%) for Cu – 12.1% Al – 4.1% Zn alloy rolled either at RT or LNT.<sup>[39]</sup>

The effect of AH was also observed for nanostructured brass (Cu-Zn alloy) powder particles doped with 5 at% Zr and milled at LNT.<sup>[40]</sup> Although the particle size was hundreds of microns, the internal microstructure was nanocrystalline. After annealing at 473 K for 1 h, the hardness increased from  $\approx 3200$  to  $\approx 4300$  MPa. Further increase in the temperature of heat treatment yielded gradual decrease in hardness; however, it remained higher than the initial value up to 1073 K.<sup>[40]</sup> The reason of this

very great AH effect was not studied. The segregation of Zr at grain boundaries and a possible formation of a Zr-containing intermetallic phase were listed as potential reasons of AH. It should be noted that a recent study proposed that solute segregation to grain boundaries in nanocrystalline SPD-processed alloys during heat treatments is not the reason of AH.<sup>[67]</sup> It is necessary only for the stabilization of the nanostructure at the beginning of annealing but not the origin of AH but rather the annihilation of mobile dislocations and the grain boundary relaxation in the stabilized nanostructure caused hardening. Indeed, it was shown that the decrease in the energy of grain boundaries during relaxation can yield hardening as shown by molecular dynamic simulations.<sup>[68]</sup> It was revealed that solute segregation to boundaries in solute-doped nanocrystalline Cu with the grain size of 8 nm can result in grain boundary relaxation, which was accompanied by the decrease in grain boundary energy. The difference between the solute and solvent atomic radii influenced this effect: the larger the size mismatch, the higher the grain boundary energy decrease. The relaxed grain boundaries with lower energies led to a more difficult grain boundary sliding and grain rotation during deformation, yielding a higher yield strength.<sup>[68]</sup>

AH can also occur in medium entropy and high entropy alloys (MEAs and HEAs). For instance, 3 passes of ECAP at RT on CoCrNi MEA led to the grain refinement to  $\approx 126$  nm.<sup>[41]</sup> Then, annealing at 773 K for 1 h resulted in an increase in the yield strength, ultimate tensile strength, and hardness by 9%, 25%, and 14%, respectively (Table 1). This AH was explained by the formation of nanotwins and lamellas with a hexagonal structure due to the low SFE of this MEA material. The same heat-treatment for cold-rolled CoCrFeMnNi HEA caused a similar increase in the hardness (9%).<sup>[43]</sup> In this case, the AH effect was attributed to a combined effect of the formation of a long-range ordered structure, annihilation of mobile dislocations, and grain boundary relaxation. In CoCrNi MEA processed by HPT at RT, the increase in the hardness due to annealing at 773 K for 1 h was 26%.<sup>[42]</sup> This AH effect was explained by the reduced mobile dislocation density and the relaxation of grain boundaries. It is noted that the hardness of HPT-processed nanocrystalline CoCrFeMnNi HEA also increased during annealing at 723 K.<sup>[69]</sup> However, this effect was caused mainly by the formation of NiMn-, FeCo-, and Cr-rich phases in the matrix; therefore, it is not discussed as AH.

It is interesting to note that remarkable AH effect was also observed in Au nanopillars with a diameter of 300 nm and an aspect ratio of two.<sup>[70,71]</sup> First, the pillars were precompressed up to the strain of 35%. This processing resulted in a softening due to the production of mobile dislocations. This DS effect is discussed in Section 4. During subsequent annealing of the pre-deformed pillars, hardening back to the level of the pristine pillars was observed. The phenomenon of AH was attributed to two major effects: 1) annihilation of mobile dislocations by climb and 2) nucleation of immobile jogs by climb during annealing. Both processes resulted in a decrease in the mobile dislocation density, yielding hardening back to the strength of the pristine pillars.<sup>[70,71]</sup>

The increase in the yield strength or the hardness due to AH is usually not higher than 30%. In contrast, an extremely large AH effect with 162% and 90% hardness enhancement was observed

for UFG Zn – 22% Al and Zn – 22% Al – 0.3% Cu alloys, respectively.<sup>[47]</sup> The duplex microstructures of these materials containing Al and Zn phases were processed by cold rolling at RT. The grain sizes in the cold-rolled Zn – 22% Al and Zn – 22% Al – 0.3% Cu alloys were 400 and 300 nm, respectively. Annealing at 523 K resulted in a grain growth with increasing time due to the high homologous temperature (about 0.7). First, the hardness increased with increasing grain size, but after a critical grain size, the hardness started to decrease as shown in **Figure 6**. The critical grain size values were 1.8 and 0.6  $\mu\text{m}$  for Zn – 22% Al and Zn – 22% Al – 0.3% Cu alloys, respectively. As these alloys have low melting points (about 753 K), the grain boundary sliding was a main deformation mechanism in the UFG microstructures during the hardness test at RT (RT corresponds to a homologous temperature of 0.4). The increase in the grain size in the range under the critical grain size value resulted in a more difficult grain boundary sliding, leading to hardening.<sup>[47]</sup> At the same time, above the critical grain size dislocation glide inside the grains became more prevalent; therefore, the hardness decreased with the increasing grain size as suggested by the Hall-Petch relation. Due to the grain-growth during annealing, this phenomenon is not a typical AH effect.

AH has no systematic effect on the ductility of SPD-processed UFG materials. For the majority of materials, AH yielded a slight decrease in the uniform and total elongations or the ductility remained unchanged as compared with the SPD-processed state.<sup>[31,33,35,41,44]</sup> An exceptional behavior was observed for HPT-processed Ti, where the elongation to failure was improved from 12% to 20% due to annealing at the homologous temperature of  $0.30 \times T_m$ .<sup>[46]</sup> This unusual behavior has not been clarified yet.

### 3.2. Hardening Induced by Annealing of Nanocrystalline Materials Produced by Bottom-Up Methods

The AH effect was also observed in nanocrystalline metallic materials processed by bottom-up methods such as

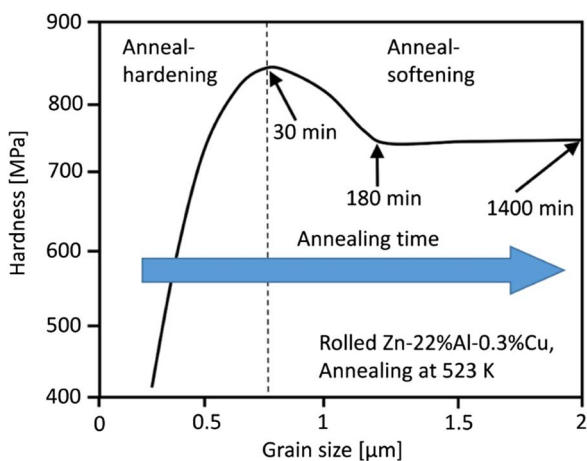


**Figure 6.** The relationship between the hardness and the grain size in Zn – 22% Al – 0.3% Cu alloy rolled at RT and subsequently annealed at 523 K for different times. Reproduced with permission.<sup>[47]</sup> Copyright 2009, Elsevier. Below the critical grain size of 0.8  $\mu\text{m}$ , annealing-hardening was observed, while above this value annealing caused softening.

electrodeposition.<sup>[29,48,49,52,54,72]</sup> For these samples, AH was usually caused by 1) grain boundary relaxation and/or 2) segregation of solute elements to boundaries and/or 3) evolution of “hard” crystallographic texture. In the first case, the emission of dislocations from the relaxed grain boundaries becomes more difficult, which makes the material more resistant to yielding under mechanical loads.<sup>[48,73,74]</sup> If the grain size is smaller than 10–20 nm, deformation mechanisms occurring in the grain boundaries (e.g., grain boundary sliding or grain rotation) become dominant. In this case, the solute segregation impedes the occurrence of these deformation mechanisms in the grain boundaries, thereby hardening the material. It should be noted that the segregation of solutes to the grain boundaries may also cause relaxation since the grain boundary energy can decrease significantly due to segregation.<sup>[68]</sup> In the third case, the original “soft” texture or the randomly oriented microstructure turns into “hard” crystallographic orientation due to annealing. For instance, if the compression axis is perpendicular to  $\langle 100 \rangle$  direction of a face-centered cubic (fcc) material, the dislocation glide is easy; thus, this is a “soft” texture. When heat treatment causes the development of a  $\langle 111 \rangle$  texture instead of  $\langle 100 \rangle$  texture, the dislocation slip becomes more difficult, leading to hardening.

The influence of alloying element concentration on the AH effect was studied in Ni(Mo) films processed by electrodeposition.<sup>[49]</sup> In the as-deposited layers, the Mo concentration varied between 0.8 and 21.5 at%. Then, the samples were annealed for 1 h at different temperatures between 300 and 1300 K. The hardness was determined as a function of annealing temperature. As examples, **Figure 7a** shows schematically the hardness versus temperature for pure Ni film and for Mo concentrations of 9.1 and 18.7 at%.<sup>[49]</sup> A maximum was observed on the hardness evolution for all Mo concentrations. **Figure 7b** shows the change in the grain size, and the temperature of the maximum hardness and the relative hardness increase in percentage as a function of the Mo content. It was found that the increase of the Mo content from 0.8 to 21.5 at% is accompanied by a decrease in the grain size from  $\approx 30$  to  $\approx 3$  nm. The peak hardness was achieved at higher temperatures for the samples with a larger solute content due to the stabilization effect of the Mo atoms on the nanostructures. **Figure 7b** also reveals that the higher the Mo content, the greater the AH effect. Indeed, for pure Ni film, the maximum hardness increase was 20%, which increased to 125% when 21.5 at% Mo was added to Ni.<sup>[49]</sup> This trend in AH is opposite to that observed for SPD-processed UFG Ni-Mo alloys. This difference was caused by the different mechanisms of plastic deformation in SPD-processed UFG alloys and electrodeposited nanomaterials. In the HPT-processed Ni alloys, the higher solute content impeded the annihilation of mobile dislocations and the clustering of the remaining dislocations during annealing, leading to a reduced AH effect.<sup>[35]</sup> In nanocrystalline Ni-Mo films, the main deformation mechanism is grain boundary sliding due to the very small grain size. During annealing, the alloying elements were segregated to grain boundaries, which hindered grain boundary sliding. This effect was more pronounced in alloys with higher solute contents, leading to a more pronounced AH.

The solute-segregation-induced AH was also observed for electrodeposited Ni – 1 wt% Fe alloy annealed at 479 K for 1 h; however, in this case, the hardness increase was only 3%.<sup>[52]</sup>

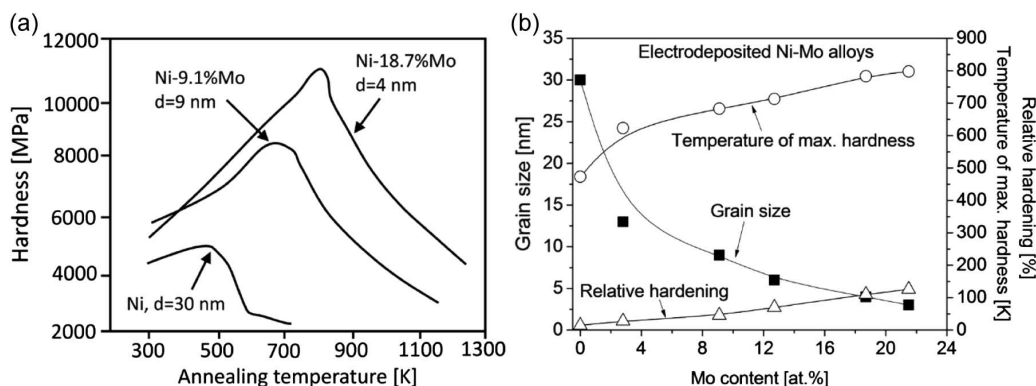


**Figure 7.** a) A schematic showing the hardness versus annealing temperature diagram for electrodeposited pure Ni film and Ni-Mo layers with the Mo concentrations of 9.1% and 18.7%. The grain sizes ( $d$ ) are also indicated at the curves. b) The change of the grain size, the temperature of maximum hardness, and the relative hardness increase in percentage as a function of Mo content for electrodeposited Ni-Mo layers. Reproduced with permission.<sup>[49]</sup> Copyright 2017, American Association for the Advancement of Science.

The grain size of this material was  $\approx 16$  nm. The AH effect was observed just before the grain size started to grow during annealing. The effect of AH was explained by the segregation of Fe, C, and O solutes to grain boundaries as revealed by atom probe tomography.

Grain boundary relaxation has a significance in the increase in hardness during annealing of electroplated films. This effect was demonstrated on nanocrystalline Ni – 15 wt% Fe and Ni – 23 wt% Fe alloys processed by electrodeposition.<sup>[53,54]</sup> The as-deposited Ni – 23 wt% Fe alloy can be characterized with an (100) out-of-plane texture, an average grain size of  $\approx 22$  nm, and a homogeneous distribution of Ni and Fe. At the same time, the sulfur impurity was segregated at the grain boundaries: about 110 and 500 ppm were detected in the grain interiors and the grain boundaries, respectively. Annealing at 523 K for 1.5 h resulted in an increase in the compressive yield strength by 27% (Table 1). At the same time, neither the grain size nor the spatial distribution of elements changed during the heat treatment. Thus, it was concluded that grain boundary relaxation caused the AH effect.<sup>[54]</sup> This relaxation made the boundaries more ordered, thereby reducing their nonequilibrium nature. It is believed that in nanocrystalline materials dislocations are not stored in the grain interiors, but rather dislocations are accumulated in the vicinity of grain boundaries. The grain boundary relaxation may be accompanied by the annihilation of these dislocations. Indeed, the dislocation density decreased from  $\approx 22$  to  $\approx 5 \times 10^{14} \text{ m}^{-2}$  in Ni – 23 wt% Fe alloy during annealing. The emission of dislocations from the relaxed boundaries is more difficult, thereby increasing the yield strength. Similar grain boundary relaxation in electrodeposited nanocrystalline Ni – 15 wt% Fe alloy with a grain size of  $\approx 9$  nm annealed at 523 K for 1.5 h led to an AH effect of  $\approx 16\%$ .<sup>[53]</sup> Table 1 reveals that the same concentration of Mo in Ni resulted in a much higher AH effect than that observed for Ni-Fe alloys, most probably due to the smaller grain size in Ni-Mo alloys. It should be noted, however, that another study revealed the occurrence of sulfur and carbon segregation to the grain boundaries during annealing of an electroplated Ni with the grain size of 15 nm, which was accompanied by a hardness enhancement of  $\approx 18\%$ .<sup>[50]</sup> In electrodeposited

nanocrystalline Ni – 1.2 wt% P layer with a grain size of 10 nm, the segregation of phosphorus to grain boundaries and the grain boundary relaxation caused a hardening of 47% as shown in Table 1.<sup>[51]</sup>

In general, it was found that the type of solute atoms influences strongly the AH effect in Ni electrodeposits. For instance, Fe and W alloying resulted in a lower relative increase in hardness or yield strength than Mo solutes with the same concentration (Table 1). In the case of iron, its less effectivity can be explained with the similar sizes of Ni and Fe atoms. Comparing Mo and W alloying, the diffusivity of Mo is higher than that for W in Ni; therefore, its segregation to the grain boundaries in Ni electrodeposits may occur before grain growth starts during annealing.<sup>[75]</sup> Therefore, the AH effect is more pronounced for a certain concentration of Mo in Ni than for Fe or W alloying (Table 1). For instance, for electrodeposited Ni – 21.5% Mo alloy with a grain size of  $\approx 3$  nm, the AH effect was much higher ( $\approx 126\%$ ) than that for Ni – 21% W alloy ( $\approx 20\%$ ) with the same grain size (Figure 8).<sup>[49,56]</sup> It should be noted that the annealing temperature was higher for the Ni – 21.5% Mo alloy (798 K) than

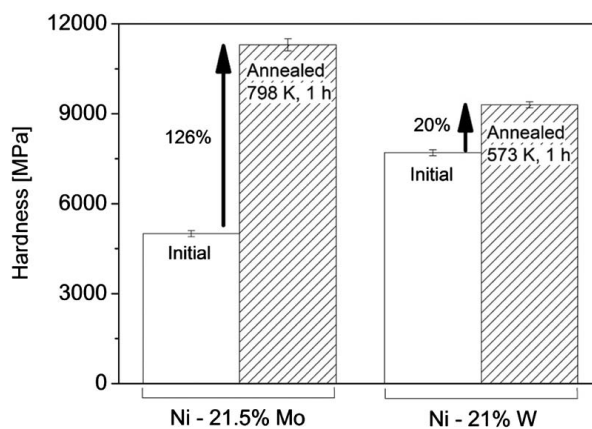


**Figure 8.** The AH effect for electrodeposited Ni – 21.5% Mo alloy with a grain size of  $\approx 3$  nm and that for Ni – 21% W alloy ( $\approx 20\%$ ) with the same grain size. Data were taken from the references<sup>[49,56]</sup>

for the Ni – 21% W alloy (573 K), which may influence the hardening effect. However, even if 573 K was selected for the heat treatment temperature of Ni – 21.5% Mo alloy, the AH effect would be higher ( $\approx 60\%$ ) for this alloy than that for Ni – 21% W alloy.<sup>[49]</sup>

The kinetics of grain boundary relaxation during annealing of Ni – 21% W alloy was studied in the temperature range between 423 and 573 K.<sup>[56]</sup> It was found that the hardness increased linearly with the heat treatment time and saturated after 10–300 min, depending on the temperature as shown in **Figure 9**. A higher temperature yielded a faster hardening. Assuming an Arrhenius relationship between the rate of hardness increase and the temperature, the activation energy of grain boundary relaxation was determined as about  $50 \text{ kJ mol}^{-1}$  for electroplated Ni – 21% W alloy. This value is significantly lower than the activation energy of grain boundary diffusion ( $115 \text{ kJ mol}^{-1}$ ).<sup>[56]</sup> At the same time, the activation energy of diffusion along triple junctions in Ni at low homologous temperatures ( $<0.33 \times T_m$ ) was also about  $50 \text{ kJ mol}^{-1}$ . It is also interesting that the rate of hardening and time for saturation were similar for both 3 and 12 nm grain sizes at all studied temperatures. These observations suggest that rapid diffusion along triple junctions is a possible mechanism of grain boundary relaxation at low temperatures. The lower the grain size, the larger the strengthening effect caused by the grain boundary relaxation.

**Figure 10** shows the relative hardening achieved during annealing for UFG and nanomaterials processed either by top-down or bottom-up methods. The data were taken from Table 1. In the grain size regime between 10 and 1000 nm, the relative hardening varies between 3% and 30%, and its value does not show any correlation with the grain size. At the same time, for electrodeposited layers with very low grain sizes (3–6 nm), an extremely large AH effect with the values above 60% was observed. It should be noted, however, that beside the grain size the relative hardening was also influenced by the type of alloying elements in the electrodeposits. For instance, Figure 10 reveals that Mo addition is more effective in AH than alloying with W even if the grain size is the same for both films. Very large hardening was also observed for SPD-processed UFG Zn-alloys with

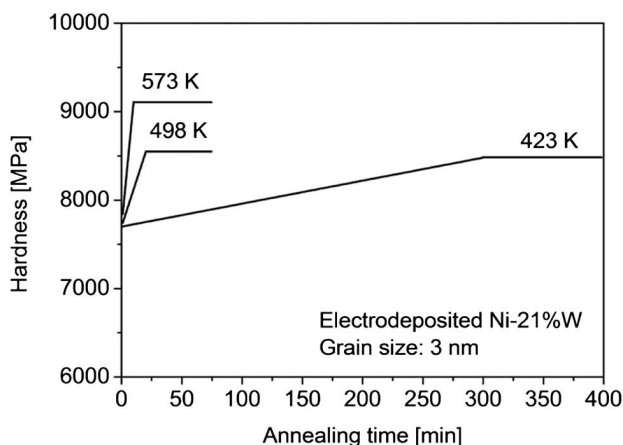


**Figure 9.** The hardness versus the annealing time for electrodeposited Ni – 21% W alloy heat treated at the temperatures of 423, 498, and 573 K. Data were taken from the references<sup>[56]</sup>

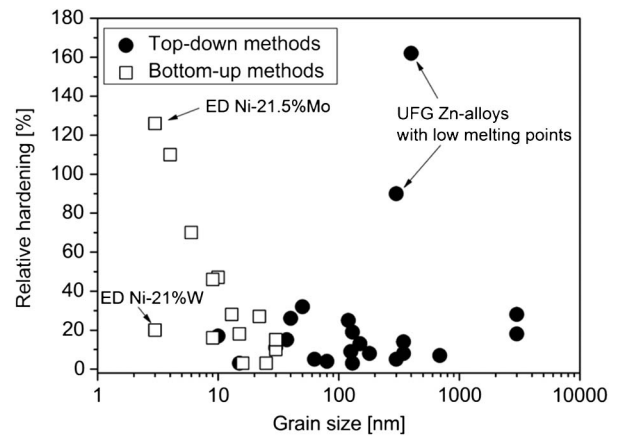


**Figure 10.** The relative AH versus the grain size for UFG and nanomaterials processed by top-down and bottom-up methods. The data were taken from Table 1.

low melting points. In these materials, the deformation mechanisms occurring at the grain boundaries are prevalent during room-temperature straining. Annealing of these materials yielded considerable grain growth, thereby reducing the role of grain boundary sliding in plasticity, which led to hardening. It should be noted, however, that this is a special case as in the majority of AH effects grain coarsening did not occur.

#### 4. Deformation-Induced Softening in Anneal-Hardened UFG Materials

For an UFG or nanocrystalline material hardened by annealing, subsequent plastic deformation may yield softening. This DS effect was observed on a 99.2% pure Al processed by ARB at RT.<sup>[29,33]</sup> Annealing at 423 K for 30 min resulted in an increase in the yield strength from 259 to 281 MPa. Then, subsequent cold rolling with a thickness reduction of 15% led a restoration of the lower yield strength. In these samples, the thickness of the lamellar grains was about 200 nm; therefore, dislocation glide was the main deformation mechanism. Thus, cold rolling after annealing caused an increase in the density of mobile dislocations, leading to a softening in the sample hardened formerly by annealing. It should be noted that if the thickness reduction of cold rolling increased from 15% to 50%, the yield strength increased back to the value observed after annealing (to about 300 MPa). This effect was explained by clustering of dislocations formed during rolling after annealing. A clustered dislocation structure has a higher hardening effect than that for a uniform dislocation distribution as discussed in Section 3.1.

It was shown in Section 3.1 that compressed single crystal Au nanopillars with a diameter of 300 nm exhibited hardening after annealing due to the formation of short jogs on dislocations.<sup>[70,71]</sup> Additional compression after annealing resulted in a vanish of these jogs, leading to a restoration of the lower original yield strength measured on the pristine pillars before annealing. Thus, DS effect was detected on the heat-treated nanopillars.

DS was also observed for annealed nanocrystalline HEA samples.<sup>[69]</sup> This effect was attributed to the deformation-induced dissolution of NiMn- and FeCo-rich intermetallic

phases, which were produced during annealing. Therefore, the longer the annealing time, the more pronounced the DS effect. The destabilization of precipitates was explained by the accumulation of dislocations at the matrix/particle interfaces, which may increase in the interface energy.<sup>[69]</sup>

It should be noted that SPD-processing of materials with low melting temperatures can cause DS effects without any preliminary annealing. This phenomenon was observed on pure UFG Al, In, Sn, Pb, Zn metals, and an Al-Zn alloy.<sup>[76–80]</sup> The low melting points and the UFG microstructures of these SPD-processed materials promote the occurrence of grain boundary sliding during hardness measurement at RT. Therefore, these materials show softer plastic behavior compared with their coarse-grained counterparts before SPD-processing. It should be noted that this DS effect depends on the purity level of the material. For instance, in Al processed by HPT, DS was observed only if the purity level reached 6N. In this material, the grain size was refined gradually from  $\approx 1$  mm to  $\approx 20$   $\mu$ m with increasing the shear strain.<sup>[79]</sup> In the vicinity of the center of the disk processed for 1/8 HPT turn (for shear strains lower than about one), the hardness increased in accordance with the Hall-Petch relationship (**Figure 11**). At the same time, for high strains, the hardness was lower than that for the initial annealed state despite the much smaller grain size. This inverse Hall-Petch behavior for 6N Al was explained by the increased role of grain boundary sliding in plastic deformation. Indeed, grain boundary sliding may become a prevalent deformation mechanism in SPD-processed Al even at RT.<sup>[80]</sup> After 1 turn of HPT, the hardness of 6N purity Al was smaller in the whole disk than that for the initial coarse-grained material (**Figure 11**). HPT-induced DS effect was also observed for a supersaturated solid solution Al – 30% Zn alloy.<sup>[81]</sup> In this case, DS was caused by the wetting of grain boundaries with a  $\approx 3$  nm thick Zn-rich layer, which resulted in an easier plasticity. DS effect without annealing was also detected in other deformed low-melting-point alloys such as cold-rolled Zn – 22% Al and Zn – 22% Al – 0.3% Cu alloys having a duplex microstructure with the grain size of 300–400 nm.<sup>[47]</sup>

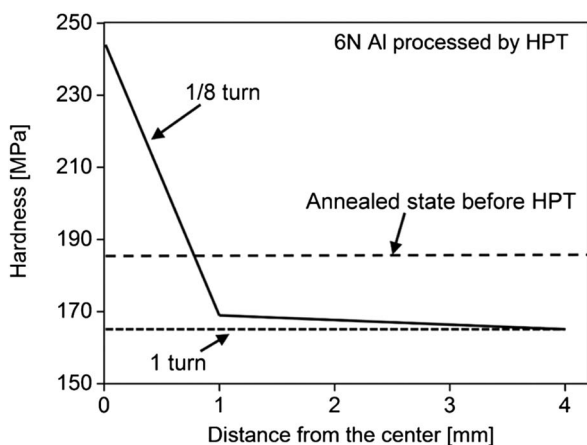


**Figure 11.** The hardness as a function of the distance from the disk center for HPT-processed 6N purity Al after 1/8 and 1 turns. Reproduced with permission.<sup>[79]</sup> Copyright 2017, Elsevier.

## 5. Summary

In this article, the AH effect occurring in UFG and nanomaterials was overviewed. This phenomenon was observed in both SPD-processed UFG materials and nanocrystalline samples manufactured by bottom-up techniques. In most cases, the highest hardening was measured after short annealing (the duration is not higher than 1 h) at the homologous temperatures between  $0.35$  and  $0.45 \times T_m$ , where  $T_m$  is the melting point. This temperature range corresponds to about 400–600 K. Due to the moderate temperatures of AH, grain growth and recrystallization are usually avoided.

For SPD-processed UFG materials, the hardening is usually caused by the annihilation of mobile dislocations inside the grains and their clustering into low energy configurations such as low-angle grain boundaries. In addition, the relaxation of non-equilibrium grain boundaries may also contribute to AH since this relaxation leads to a more difficult emission of dislocations from the boundaries. The clustering of excess vacancies may also yield AH effect since the vacancy clusters can impede the motion of dislocations. The relative increase in the room-temperature yield strength or hardness caused by the AH effect is usually between 3% and 30%, and its value does not show any correlation with the grain size in the grain size regime between 10 and 1000 nm. A very large AH effect with the relative hardening of 90–160% was observed for SPD-processed UFG Zn-alloys annealed at the homologous temperature of  $\approx 0.7$ . Due to the high homologous temperature of the heat treatment, considerable grain growth was observed after annealing. Due to the low melting points and the UFG microstructures of these materials, the deformation mechanisms occurring at the grain boundaries are prevalent in room-temperature straining of the SPD-processed samples. The grain-growth during annealing of these materials yielded a reduced role of grain boundary sliding in plasticity, which led to hardening. It should be noted, however, that this is a special case as in the majority of AH effects grain coarsening did not occur.

For nanocrystalline samples processed by bottom-up methods, the AH effect was caused by the grain boundary relaxation and the segregation of solutes to grain boundaries. Extremely large AH effect with the values above 60% was observed for electrodeposited layers with very low grain sizes (3–6 nm). Apart from the grain size, the relative hardening was also influenced by the type of the alloying elements. The highest AH effect with the value of 126% was observed for Ni – 21.5 at% Mo layer processed by electrodeposition.

Plastic deformation of the annealed UFG materials can yield a restoration of the lower yield strength and hardness observed before annealing. This DS effect can be attributed to the increase in the density of mobile dislocations during deformation of the annealed samples.

It should be emphasized that AH effect results in further strengthening of UFG or nanocrystalline materials without considerable deterioration of ductility. Therefore, this phenomenon has a great practical significance since it can lead to a better mechanical performance of nanomaterials. The improved strength extends the applicability of UFG materials in the industry. It is noted, however, that the strength increase is not very high as usually it varies between 3% and 30%. Extremely large

AH effect was observed mainly on nanocrystalline films with very small grain sizes (<10 nm) processed by bottom-up methods. Therefore, a great potential of the AH effect in the development of ultrahard coatings can be visualized.

It is also worth noting that UFG materials usually have low ductility and AH does not improve this feature of these materials that limits its industrial impact. However, an important advantage of AH is that this effect is universal, i.e., it was observed for both pure UFG materials and alloys with different crystal structures processed either by bottom-up or top-down methods. This universality of AH can be explained by the fact that the phenomenon is basically caused by the relaxation of the defect structure that may occur in any material with high defect densities. Therefore, AH processing of UFG and nanomaterials can be used in many different industrial applications (e.g., manufacturing surgical implants or hard coatings).

Although, many research efforts have been invested in the study of the AH effect, some open questions still remained. For instance, as more than one simultaneous process occurs in the UFG microstructures during annealing (e.g., annihilation of mobile dislocations and grain boundary relaxation), their relative contributions to the hardening must be clarified. Moreover, as AH effect has a great potential for practical applications, a further research direction may be the study of this phenomenon in fine-grained materials processed by industrial techniques, such as caliber rolling or drawing. In addition, until now, only the mechanical performance of the materials treated by AH was investigated, but for the possible applications, the study of the influence of AH on the functional behaviors (e.g., electric, magnetic, and corrosion properties) is also necessary.

## Acknowledgements

This work was financed partly by the Ministry of Human Capacities of Hungary within the ELTE University Excellence program (1783-3/2018/FEKUTSRAT).

## Conflict of Interest

The authors declare no conflict of interest.

## Keywords

annealing-induced hardening, dislocations, grain boundaries, nanocrystalline materials, segregation

Received: May 6, 2019

Revised: May 30, 2019

Published online: August 8, 2019

- 
- [1] G. I. Taylor, *J. Inst. Metall.* **1938**, 62, 307.  
 [2] B. B. Rath, M. A. Imam, C. S. Pande, *Mater. Chem. Phys.* **2000**, 1, 61.  
 [3] K. Lu, L. Lu, S. Suresh, *Science* **2009**, 324, 349.  
 [4] E. O. Hall, *Proc. Phys. Soc. London B* **1951**, 64, 747.  
 [5] N. J. Petch, *J. Iron Steel Inst.* **1953**, 174, 25.  
 [6] T. G. Langdon, *Acta Mater.* **2013**, 61, 7035.  
 [7] R. Z. Valiev, A. P. Zhilyaev, T. G. Langdon, *Bulk Nanostructured Materials, Fundamentals and Applications*, John Wiley & Sons, Inc., Hoboken, New Jersey **2014**.

- [8] M. A. Meyers, A. Mishra, D. J. Benson, *Prog. Mater. Sci.* **2006**, 51, 427.  
 [9] J. Gubicza, *Defect Structure and Properties of Nanomaterials*, Woodhead Publishing, Duxford, UK **2017**.  
 [10] M. F. Ashby, R. A. Verall, *Acta Metall.* **1973**, 21, 149.  
 [11] P. Yavari, T. G. Langdon, *J. Mater. Sci. Lett.* **1983**, 2, 522.  
 [12] M. Bader, G. T. Eldis, H. Warlimont, *Metall. Trans. A* **1976**, 7, 249.  
 [13] S. Miura, T. Tajima, *Met. Sci.* **1978**, 12, 183.  
 [14] J. M. Vitek, H. Warlimont, *Metall. Mater. Trans. A* **1979**, 10, 1889.  
 [15] R. W. Cahn, R. G. Davies, *Phil. Mag.* **1960**, 5, 1119.  
 [16] J. M. Popplewell, J. Crane, *Metall. Mater. Trans. B* **1971**, 2, 3411.  
 [17] R. R. Hasiguti, *J. Jpn. Inst. Metals* **1955**, 19, 103.  
 [18] Z. R. Zeng, Y. M. Zhu, M. Z. Bian, S. W. Xu, C. H. J. Davies, N. Birbilis, J. F. Nie, *Scripta Mater.* **2015**, 107, 127.  
 [19] L. Zhao, Y. Xin, F. Guo, H. Yu, Q. Liu, *Mater. Sci. Eng. A* **2016**, 654, 344.  
 [20] J. Capek, K. Mathis, B. Clausen, J. Straska, P. Beran, P. Lukas, *Mater. Sci. Eng. A* **2014**, 602, 25.  
 [21] Y. Xin, X. Zhou, H. Chen, J. F. Nie, H. Zhang, Y. Zhang, Q. Liu, *Mater. Sci. Eng. A* **2014**, 594, 287.  
 [22] J. F. Nie, Y. M. Zhu, J. Z. Liu, X. Y. Fang, *Science* **2013**, 340, 957.  
 [23] J. Chen, Z. Q. Wang, X. G. Ma, X. H. Wang, Y. P. Lei, W. Yan, *J. Alloys Compd.* **2015**, 642, 92.  
 [24] V. Viswanathan, T. Laha, K. Balani, A. Agarwal, S. Seal, *Mater. Sci. Eng. R* **2006**, 54, 121.  
 [25] R. Z. Valiev, F. Chmelik, F. Bordeaux, G. Kapelski, B. Baudelet, *Scripta Metall. Mater.* **1992**, 27, 855.  
 [26] J. R. Weertman, *Mater. Sci. Eng. A* **1993**, 166, 161.  
 [27] J. Languillaume, F. Chmelik, G. Kapelski, F. Bordeaux, A. A. Nazarov, G. Canova, C. Esling, R. Z. Valiev, B. Baudelet, *Acta Metall. Mater.* **1993**, 41, 2953.  
 [28] A. A. Popov, I. Y. Pyshmintsev, S. L. Demakov, A. G. Illarionov, T. C. Lowe, A. V. Sergeeva, R. Z. Valiev, *Scripta Mater.* **1997**, 37, 1089.  
 [29] X. Huang, N. Hansen, N. Tsuji, *Science* **2006**, 312, 249.  
 [30] N. Kamikawa, X. Huang, N. Tsuji, N. Hansen, *Acta Mater.* **2009**, 57, 4198.  
 [31] W. Zeng, Y. Shen, N. Zhang, X. Huang, J. Wang, G. Tang, A. Shan, *Scripta Mater.* **2012**, 66, 147.  
 [32] L. H. Su, C. Lu, A. K. Tieu, L. Z. He, Y. Zhang, D. Wexler, *Mater. Lett.* **2011**, 65, 514.  
 [33] X. Huang, *Scripta Mater.* **2009**, 60, 1078.  
 [34] N. Jia, X. Zhao, D. Song, M. H. Zhou, Y. D. Wang, *Mater. Sci. Eng. A* **2010**, 527, 1143.  
 [35] J. Gubicza, P. H. R. Pereira, G. Kapoor, Y. Huang, V. Subramanya Sarma, T. G. Langdon, *Adv. Eng. Mater.* **2018**, 20, 1800184.  
 [36] T. D. Shen, R. B. Schwarz, S. Feng, J. G. Swadener, J. Y. Huang, M. Tang, J. Z. Zhang, S. C. Vogel, Y. S. Zhao, *Acta Mater.* **2007**, 55, 5007.  
 [37] J. Tao, G. Chen, W. Jian, J. Wang, Y. Zhu, X. Zhu, T. G. Langdon, *Mater. Sci. Eng. A* **2015**, 628, 207.  
 [38] Y. L. Gong, S. Y. Ren, S. D. Zeng, X. K. Zhu, *Mater. Sci. Eng. A* **2016**, 659, 165.  
 [39] S. Zhou, W. Lv, P. Li, Y. Gong, J. Tao, L. Cheng, X. Zhu, *Mater. Sci. Eng. A* **2014**, 609, 217.  
 [40] M. A. Atwater, H. Bahmanpour, R. O. Scattergood, C. C. Koch, *J. Mater. Sci.* **2013**, 48, 220.  
 [41] H. W. Deng, Z. M. Xie, B. L. Zhao, Y. K. Wang, M. M. Wang, J. F. Yang, T. Zhang, Y. Xiong, X. P. Wang, Q. F. Fang, C. S. Liu, *Mater. Sci. Eng. A* **2019**, 744, 241.  
 [42] S. Praveen, J. W. Bae, P. Asghari-Rad, J. M. Park, H. S. Kim, *Mater. Sci. Eng. A* **2018**, 734, 338.  
 [43] J. Gu, M. Song, *Scripta Mater.* **2019**, 162, 345.  
 [44] A. Y. Volkov, I. V. Kliukin, *Mater. Sci. Eng. A* **2015**, 627, 56.

- [45] L. Zhiming, F. Liming, F. Bin, S. Aidang, *Mater. Sci. Eng. A* **2012**, 558, 309.
- [46] R. Z. Valiev, A. V. Sergueeva, A. K. Mukherjee, *Scripta Mater.* **2003**, 49, 669.
- [47] C. F. Yang, J. H. Pan, T. H. Lee, *J. Alloys Compd.* **2009**, 468, 230.
- [48] Y. M. Wang, S. Cheng, Q. M. Wei, E. Ma, T. G. Nieh, A. Hamza, *Scripta Mater.* **2004**, 51, 1023.
- [49] J. Hu, Y. N. Shi, X. Sauvage, G. Sha, K. Lu, *Science* **2017**, 355, 1292.
- [50] X. F. Zhang, T. Fujita, D. Pan, J. S. Yu, T. Sakurai, M. W. Chen, *Mater. Sci. Eng. A* **2010**, 527, 2297.
- [51] L. Chang, P. W. Kao, C.-H. Chen, *Scripta Mater.* **2007**, 56, 713.
- [52] N. Zhang, S. B. Jin, G. Sha, J. K. Yu, X. C. Cai, C. C. Du, T. D. Shen, *Mater. Sci. Eng. A* **2018**, 735, 354.
- [53] F. Ebrahimi, H. Q. Li, *J. Mater. Sci.* **2007**, 42, 1444.
- [54] H. Li, F. Jiang, S. Ni, L. Li, G. Sha, X. Liao, S. P. Ringer, H. Choo, P. K. Liaw, A. Misra, *Scripta Mater.* **2011**, 65, 1.
- [55] M. Haj-Taieb, A. S. M. A. Haseeb, J. Caulfield, K. Bade, J. Aktaa, K. J. Hemker, *Microsyst. Technol.* **2008**, 14, 1531.
- [56] T. J. Rupert, J. R. Trelewicz, C. A. Schuh, *J. Mater. Res.* **2012**, 27, 1285.
- [57] S. Ozerinc, K. Tai, N. Q. Vo, P. Bellon, R. S. Averbach, W. P. King, *Scripta Mater.* **2012**, 67, 720.
- [58] A. Hasnaoui, H. Van Swygenhoven, P. M. Derlet, *Acta Mater.* **2002**, 50, 3927.
- [59] Y. Z. Tian, J. Freudenberger, R. Pippan, Z. F. Zhang, *Mater. Sci. Eng. A* **2013**, 568, 184.
- [60] L. X. Sun, N. R. Tao, M. Kuntz, J. Q. Yu, K. Lu, *J. Mater. Sci. Technol.* **2014**, 30, 731.
- [61] K. A. Darling, L. J. Kecskes, M. Atwater, J. Semones, R. O. Scattergood, C. C. Koch, *J. Mater. Res.* **2013**, 8, 1813.
- [62] G. Kapoor, Y. Huang, V. Subramanya Sarma, T. G. Langdon, J. Gubicza, *Mater. Char.* **2017**, 130, 56..
- [63] J. Gubicza, *X-Ray Line Profile Analysis in Materials Science*, IGI-Global, Hershey, PA, USA **2014**.
- [64] J. R. Bowen, *Mater. Sci. Eng. A* **2008**, 483–484, 231.
- [65] B. A. Greenberg, O. V. Antonova, A. M. Vlasova, M. A. Ivanov, *Crystallogr. Rep.* **2012**, 57, 541.
- [66] Z. Horita, T. Fujinami, M. Nemoto, T. G. Langdon, *Metall. Mater. Trans. A* **2000**, 31, 691.
- [67] O. Renk, A. Hohenwarter, K. Eder, K. S. Kormout, J. M. Cairney, R. Pippan, *Scripta Mater.* **2015**, 95, 27.
- [68] N. Q. Vo, J. Schafer, R. S. Averbach, K. Albe, Y. Ashkenazy, P. Bellon, *Scripta Mater.* **2011**, 65, 660.
- [69] D. H. Lee, J. A. Lee, Y. Zhao, Z. Lu, J. Y. Suh, J. Y. Kim, U. Ramamurty, M. Kawasaki, T. G. Langdon, J. Jang, *Acta Mater.* **2017**, 140, 443.
- [70] S. W. Lee, S. M. Han, W. D. Nix, *Acta Mater.* **2009**, 57, 4404.
- [71] F. X. Liu, Z. L. Liu, X. Y. Pei, J. Q. Hu, Z. Zhuang, *Int. J. Plasticity* **2017**, 99, 102.
- [72] X. Y. Zhang, Q. Liu, X. L. Wu, A. W. Zhu, *Appl. Phys. Lett.* **2008**, 93, 261907.
- [73] M. M. Abramova, N. A. Enikeev, R. Z. Valiev, A. Etienne, B. Radiguet, Y. Ivanisenko, X. Sauvage, *Mater. Lett.* **2014**, 136, 349.
- [74] R. Z. Valiev, N. A. Enikeev, M. Y. Murashkin, V. U. Kazykhanov, X. Sauvage, *Scripta Mater.* **2010**, 63, 949.
- [75] S. J. B. Kurz, C. Ensslen, U. Welzel, A. Leineweber, E. J. Mittemeijer, *Scripta Mater.* **2013**, 69, 65.
- [76] K. Edalati, Z. Horita, *Mater. Sci. Eng. A* **2011**, 528, 7514.
- [77] K. Edalati, J. M. Cubero-Sesin, A. Alhamidi, I. F. Mohamed, Z. Horita, *Mater. Sci. Eng. A* **2014**, 613, 103.
- [78] B. Srinivasarao, A. P. Zhilyaev, T. G. Langdon, M. T. Perez-Prado, *Mater. Sci. Eng. A* **2013**, 562, 196.
- [79] Y. Ito, K. Edalati, Z. Horita, *Mater. Sci. Eng. A* **2017**, 679, 428.
- [80] N. Q. Chinh, P. Szommer, Z. Horita, T. G. Langdon, *Adv. Mater.* **2006**, 18, 34.
- [81] N. Q. Chinh, P. Jenei, J. Gubicza, E. V. Bobruk, R. Z. Valiev, T. G. Langdon, *Mater. Lett.* **2017**, 186, 334.